

UNIVERSITÀ DI PISA

DIPARTIMENTO DI FISICA

Laurea Magistrale in Fisica

**Measurement of the V_{cb} CKM element
from $t\bar{t}$ semileptonic decays at CMS**

Relatore:

Prof. Paolo Azzurri

Candidato:

Piero Viscone

ANNO ACCADEMICO 2022/2023

2 Abstract

3 The Standard Model of particle physics has been very successful. But there are problems. They
4 can be explained by new exotic particles.

5 A search is presented for a new exotic particle. Events with jets are considered. A novel
6 technique is used. The search is based on Run-2 proton-proton collision data at a center-of-mass
7 energy of 13 TeV recorded with the CMS detector corresponding to an integrated luminosity of
8 137.1 fb^{-1} .

9 Upper limits are set on the production cross section of a new exotic particle as a function of
10 mass. Results are compared with theoretical predictions to obtain lower limits on the mass. At
11 95% confidence level, new exotic particles are excluded for masses below X GeV.

Contents

13	1 Introduction	1
14	2 The Standard Model	2
15	2.1 The Standard Model	2
16	2.1.1 The Standard Model Lagrangian	2
17	2.1.2 The gauge sector	2
18	2.1.3 The Yukawa sector	5
19	2.1.4 CKM matrix	5
20	2.2 Higgs	6
21	2.3 The physics of proton-proton collisions	6
22	3 Beyond the Standard Model	8
23	4 The CMS Experiment	10
24	4.1 The Large Hadron Collider	10
25	4.1.1 Luminosity	10
26	4.2 The CMS detector	12
27	4.2.1 Coordinate system	13
28	4.2.2 The solenoid magnet & flux-return yoke	13
29	4.2.3 The pixel tracker	13
30	4.2.4 The silicon strip tracker	13
31	4.2.5 The electromagnetic calorimeter	13
32	4.2.6 The hadronic calorimeter	13
33	4.2.7 The muon system	13
34	4.2.8 The trigger system	15
35	5 Object & Event Reconstruction	16
36	5.1 Principles of particle identification	16
37	5.2 Particle-flow algorithm	16
38	5.3 Primary vertex	16
39	5.4 Electrons	16
40	5.5 Muons	16
41	5.6 Hadronically Decayed τ Leptons	18
42	5.7 Jets	18
43	5.8 Bottom quark identification	18
44	5.9 Missing transverse energy	20
45	6 Data sets & Simulated Samples	21
46	6.1 Data sets	21
47	6.2 Event simulation	21

48	6.3 Backgrounds	21
49	6.3.1 Simulated backgrounds	21
50	6.3.2 Cross sections	24

51	7 Event Selection	25
----	--------------------------	-----------

52	References	26
----	-------------------	-----------

53 1 Introduction

54 Over the last 100 years, physicists have made large strides in understanding the natural laws
55 that govern the universe as we know it. The Standard Model (SM) of particle physics describes
56 matter and its interactions.

57 In 2012, the discovery of the Higgs boson was announced by the ATLAS and CMS experiments [1–3] at CERN’s LHC. The Higgs was 47 years before that [4, 5]. Despite its many
58 successes, there are both theoretical and experimental reasons that imply the SM is not the final
59 theory of Nature.

61 This dissertation has the following structure: Chapter 2 discusses the SM, after which Chapter
62 3 motivates the search for new hypothetical particles. Chapter 4 describes the LHC accelerator,
63 CMS detector and the data collection. Chapter 5 describes the physics objects that are
64 relevant for this thesis. After these, Chapter 7 discusses the selections.

65 2 The Standard Model

66 This chapter introduces the Standard Model (SM) of particle physics. I left a bit of text with
67 equations, citations, figures, and tables as an example of this template.

68 2.1 The Standard Model

69 A rough timeline of the experimental discovery of particles is given by Fig. 2.1. More detailed
70 historical discussions can be found in Refs. [6–8].¹

71 With a mass of $m_t \approx 172.8 \text{ GeV}$ [10, p. 32], the top quark is by far the heaviest fermion.

72 The discovery of the Higgs was announced in 2012 [1–3, 11]. A single Higgs boson is the
73 simplest and most minimal solution, although it is possible to achieve SBB with more than one
74 Higgs boson. No evidence of additional Higgs bosons have been found so far [12].

75 2.1.1 The Standard Model Lagrangian

76 The SM is encoded in the *SM Lagrangian density*. The terms of the Lagrangian density can be
77 grouped into three separate *sectors*:

$$\mathcal{L}_{\text{SM}} = \mathcal{L}_{\text{gauge}} + \mathcal{L}_{\text{Higgs}} + \mathcal{L}_{\text{Yukawa}}. \quad (2.1)$$

78 Secondly, the SM is a *gauge theory*: It has an internal symmetry that corresponds to the
79 local $\text{SU}(3)_C \times \text{SU}(2)_L \times \text{U}(1)_Y$ symmetry group. The SM gauge group is spontaneously broken
80 to

$$\text{SU}(3)_C \times \text{SU}(2)_L \times \text{U}(1)_Y \xrightarrow{\text{SSB}} \text{SU}(3)_C \times \text{U}(1)_{\text{EM}} \quad (2.2)$$

81 by the nonzero vev of the Higgs field, where $\text{U}(1)_{\text{EM}}$ is the gauge symmetry group for QED.

82 2.1.2 The gauge sector

83 The gauge sector can be written as

$$\mathcal{L}_{\text{gauge}} = \sum_f \sum_{\psi_f} \bar{\psi}_f i\gamma^\mu D_\mu \psi_f - \frac{1}{4} G_{\mu\nu}^a G_a^{\mu\nu} - \frac{1}{4} W_{\mu\nu}^i W_i^{\mu\nu} - \frac{1}{4} B^{\mu\nu} B^{\mu\nu}, \quad (2.3)$$

84 in natural units $c = \hbar = 1$ [14], and where $a = 1, \dots, 8$ and $i = 1, 2, 3$. In the first term, matter
85 is given by five fermion fields ψ_f in three generations $f = 1, 2, 3$;

$$Q_L^f = \begin{pmatrix} u_L^f \\ d_L^f \end{pmatrix}, \quad u_R^f, \quad d_R^f, \quad L_L^f = \begin{pmatrix} \nu_L^f \\ e_L^f \end{pmatrix}, \quad e_R^f. \quad (2.4)$$

86 Their Dirac adjoints are given by $\bar{\psi}_f = \psi_f^\dagger \gamma^0$.

¹prova

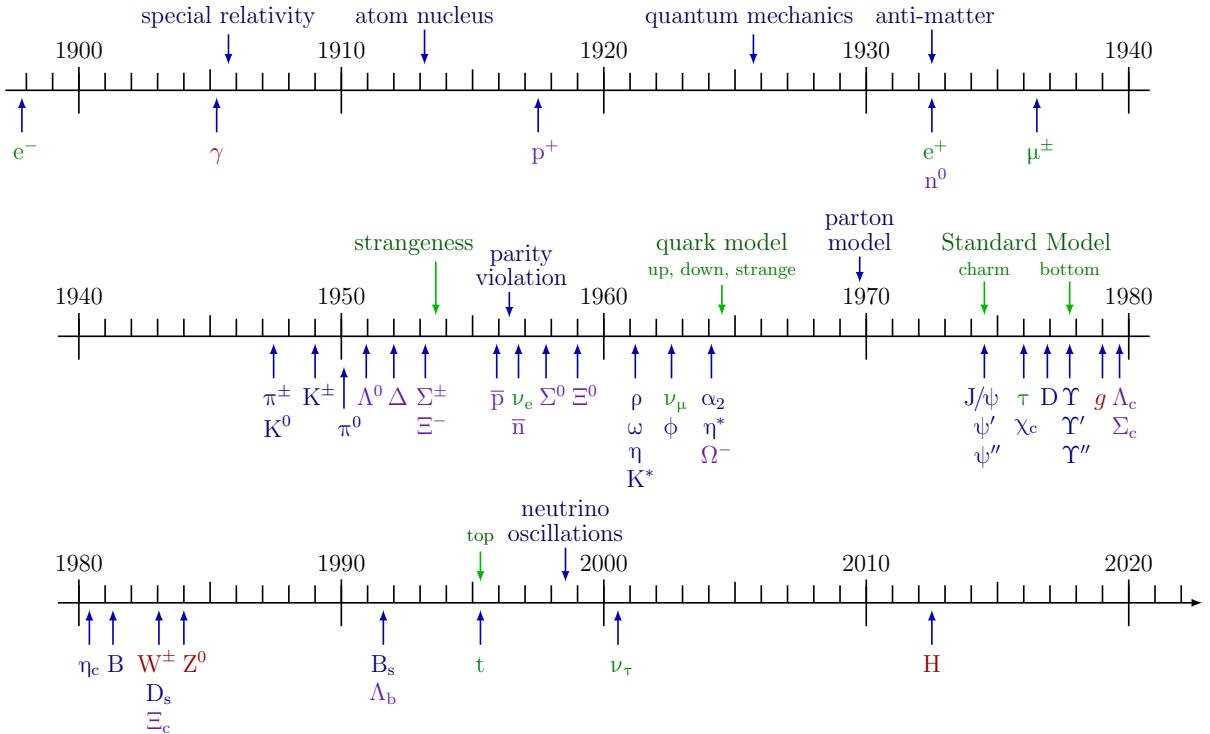


Figure 2.1: A timeline of particle physics in the last 130 years. Adapted from Ref. [9].

three generations of matter (fermions)			interactions / forces (bosons)	
I	II	III	gluon	Higgs
mass charge spin $\simeq 2.2 \text{ MeV}$ $+2/3$ $1/2$ u up	mass charge spin $\simeq 1.3 \text{ GeV}$ $+2/3$ $1/2$ c charm	mass charge spin $\simeq 173 \text{ GeV}$ $+2/3$ $1/2$ t top	0 0 1 g gluon	$\simeq 125 \text{ GeV}$ 0 0 0 H Higgs
QUARKS			0 0 1 γ photon	
d	s	b		
mass charge spin $\simeq 4.7 \text{ MeV}$ $-1/3$ $1/2$ d down	mass charge spin $\simeq 96 \text{ MeV}$ $-1/3$ $1/2$ s strange	mass charge spin $\simeq 4.2 \text{ GeV}$ $-1/3$ $1/2$ b bottom		
LEPTONS				
e	μ	τ		
mass charge spin $\simeq 0.511 \text{ MeV}$ -1 $1/2$ e electron	mass charge spin $\simeq 106 \text{ MeV}$ -1 $1/2$ μ muon	mass charge spin $\simeq 1.777 \text{ GeV}$ -1 $1/2$ τ tau	0 0 1 W W boson	
ν _e	ν _μ	ν _τ		
mass charge spin $< 1.0 \text{ eV}$ 0 $1/2$ ν_e electron neutrino	mass charge spin $< 0.17 \text{ eV}$ 0 $1/2$ ν_μ muon neutrino	mass charge spin $< 18.2 \text{ MeV}$ 0 $1/2$ ν_τ tau neutrino	0 0 1 Z Z boson	GAUGE BOSONS VECTORS SCALAR BOSONS

Figure 2.2: A table of the particles in Standard Model of particle physics and their properties. Figure adapted from Ref. [13].

Table 2.1: Summary of the representation and quantum numbers SM fields. Bold numbers indicate the dimension of the representation under the respective gauge group.

Field name	Symbol	Representations		Quantum numbers		
		SU(3) _C	SU(2) _L	T_3	$Y/2$	$Q = T_3 + Y/2$
Quark doublet	$Q_L = \begin{pmatrix} u_L \\ d_L \end{pmatrix}$	3	2	$\begin{pmatrix} +\frac{1}{2} \\ -\frac{1}{2} \end{pmatrix}$	$+\frac{1}{6}$	$\begin{pmatrix} +\frac{2}{3} \\ -\frac{1}{3} \end{pmatrix}$
Up-quark singlet	u_R	3	1	$+\frac{2}{3}$	$+\frac{2}{3}$	$+\frac{2}{3}$
Down-quark singlet	d_R	3	1	$-\frac{1}{3}$	$-\frac{1}{3}$	$-\frac{2}{3}$
Lepton doublet	$L_L = \begin{pmatrix} \nu_L \\ e_L \end{pmatrix}$	1	2	$\begin{pmatrix} +\frac{1}{2} \\ -\frac{1}{2} \end{pmatrix}$	$-\frac{1}{2}$	$\begin{pmatrix} 0 \\ -1 \end{pmatrix}$
Lepton singlet	e_R	1	1	0	-1	-1
Gluon field	G_μ^a	8	1	0	0	0
Weak gauge field	$W_\mu^i = \begin{pmatrix} W_\mu^+ \\ W_\mu^- \\ W_\mu^3 \end{pmatrix}$	1	3	$\begin{pmatrix} +1 \\ -1 \\ 0 \end{pmatrix}$	0	$\begin{pmatrix} +1 \\ -1 \\ 0 \end{pmatrix}$
Hypercharge field	B_μ	1	1	0	0	0
Higgs doublet	$\Phi = \begin{pmatrix} \phi^+ \\ \phi^0 \end{pmatrix}$	1	2	$\begin{pmatrix} +\frac{1}{2} \\ -\frac{1}{2} \end{pmatrix}$	$+\frac{1}{2}$	$\begin{pmatrix} +1 \\ 0 \end{pmatrix}$
Conjugate Higgs doublet	$\Phi^c = \begin{pmatrix} \phi^{0*} \\ \phi^- \end{pmatrix}$	1	2	$\begin{pmatrix} +\frac{1}{2} \\ -\frac{1}{2} \end{pmatrix}$	$-\frac{1}{2}$	$\begin{pmatrix} 0 \\ -1 \end{pmatrix}$

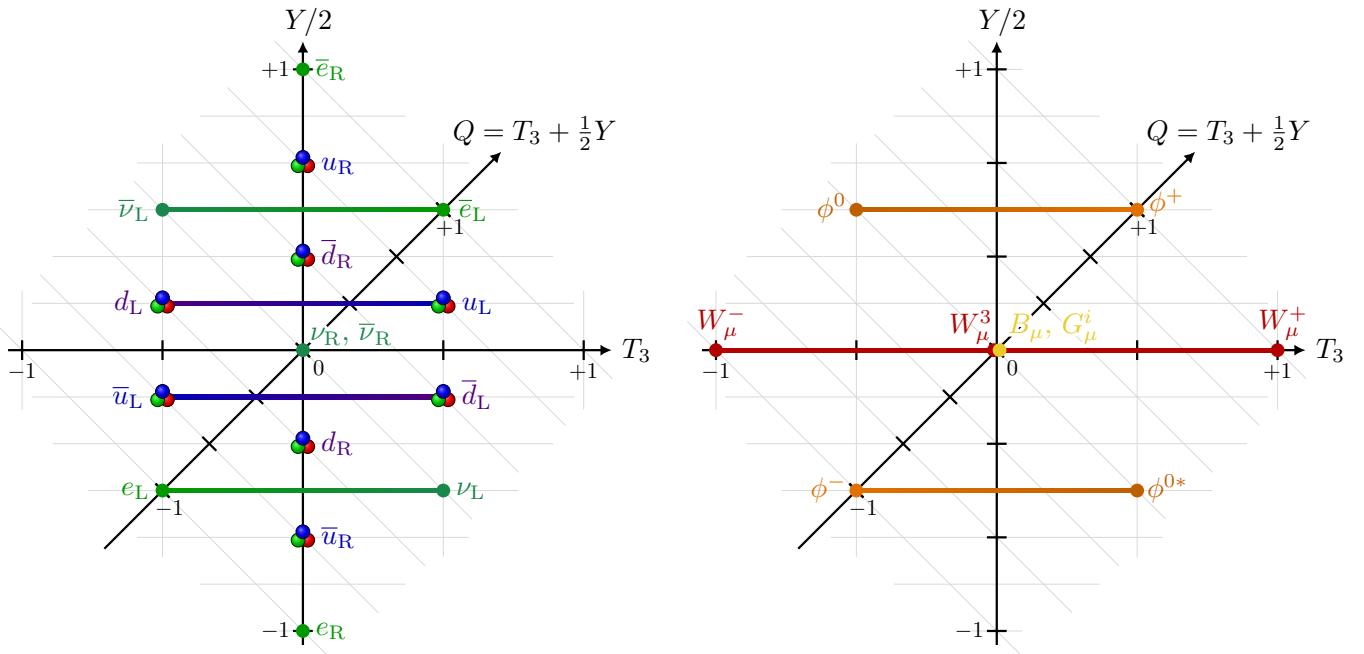


Figure 2.3: Graph of the $(T_3, Y/2)$ quantum numbers.

87 The covariant derivative

$$D_\mu = \partial_\mu + ig_s t_a G_\mu^a + ig T_i W_\mu^i + ig' \frac{Y}{2} B_\mu \quad (2.5)$$

88 where T_i and t_a are the generators for $SU(2)_L$ and $SU(3)_C$, respectively, and Y is the weak
89 hypercharge of the field that D_μ acts on.

90 Through the Higgs mechanism, the gauge bosons acquire mass and mix into the mass eigen-
91 states

$$W_\mu^\pm = \frac{W_\mu^1 \mp iW_\mu^2}{\sqrt{2}}, \quad Z_\mu = W_\mu^3 \cos \theta_W + B_\mu^3 \sin \theta_W, \quad A_\mu = W_\mu^3 \sin \theta_W - B_\mu^3 \cos \theta_W, \quad (2.6)$$

92 where W_μ^\pm are the charged W boson fields, Z_μ is the neutral Z boson field, A_μ is the photon
93 field, and θ_W is the Weinberg angle given by $\sin \theta_W = g'/\sqrt{g^2 + g'^2}$. After mixing, the new
94 covariant derivative becomes

$$D_\mu = \partial_\mu + ig_s t_a G_\mu^a + i \frac{g}{\sqrt{2}} T^+ W_\mu^+ + i \frac{g}{\sqrt{2}} T^- W_\mu^- + i \frac{g}{\cos \theta_W} (T_3 - \sin^2 \theta_W Q) Z_\mu + ieQ A_\mu, \quad (2.7)$$

95 with ladder operators $T^\pm = T_1 \pm iT_2$.

96 2.1.3 The Yukawa sector

97 In order to explain mass of the fermions,

$$\mathcal{L}_{\text{Yukawa}} = -Y_d^{fg} \bar{Q}_L^f \Phi d_R^g - Y_u^{fg} \bar{Q}_L^f \Phi^c u_R^g - Y_e^{fg} \bar{L}_L^f \Phi e_R^g + \text{h.c.}, \quad (2.8)$$

98 with the conjugate Higgs doublet $\Phi^c = i\sigma_2 \Phi^\dagger$, and unitary Yukawa matrices Y_d^{fg} , Y_u^{fg} , $Y_e^{fg} \in$
99 $U(3)$ that mixes the fermion generations. As Φ is a scalar field that forms a weak isospin doublet,

$$\Phi = \begin{pmatrix} \phi^+ \\ \phi^0 \end{pmatrix}. \quad (2.9)$$

100 Because the Higgs vev is nonzero, we can fix the $SU(2)_L$ gauge. It is convenient to choose
101 the unitary gauge

$$\Phi = \frac{1}{\sqrt{2}} \begin{pmatrix} 0 \\ v + h \end{pmatrix}, \quad (2.10)$$

102 with the vev $v \approx 246$ GeV, a real constant, and the neutral Higgs field h , a (real) scalar.
103 Therefore, after SSB, we are left with

$$\mathcal{L}_{\text{Yukawa}} = -\frac{Y_d^{fg}}{\sqrt{2}} \bar{d}_L^f (v + h) d_R^g - \frac{Y_u^{fg}}{\sqrt{2}} \bar{u}_L^f (v + h) u_R^g - \frac{Y_e^{fg}}{\sqrt{2}} \bar{e}_L^f (v + h) e_R^g + \text{h.c.} \quad (2.11)$$

104 2.1.4 CKM matrix

105 To explain the suppressed decay rate of $K^0 \rightarrow \mu^+ \mu^-$, Glashow, Iliopoulos, and Maiani used a
106 mixing matrix and proposed the existence of the charm quark [15]. This is referred to as the
107 *Glashow–Iliopoulos–Maiani (GIM) mechanism*. The mixing of two quark generations is given
108 by the *Cabibbo matrix*:

$$\begin{pmatrix} d' \\ s' \end{pmatrix} = \begin{pmatrix} \cos \theta_C & \sin \theta_C \\ -\sin \theta_C & \cos \theta_C \end{pmatrix} \begin{pmatrix} d \\ s \end{pmatrix}, \quad (2.12)$$

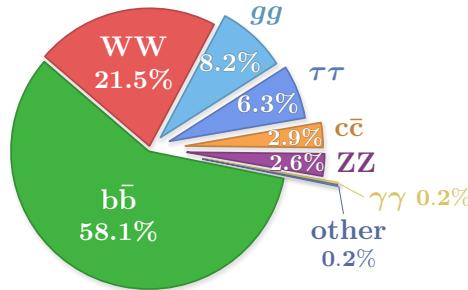


Figure 2.4: Pie chart of Higgs branching fractions.

where $|d'\rangle$ and $|s'\rangle$ represent the weak eigenstates, which are linear combinations of the mass eigenstates $|d\rangle$ and $|s\rangle$. The mixing is quantified with the *Cabibbo angle* $\theta_C \approx 13.04^\circ$.

The mixing of three generations is given by

$$\begin{pmatrix} d' \\ s' \\ b' \end{pmatrix} = \begin{pmatrix} V_{ud} & V_{us} & V_{ub} \\ V_{cd} & V_{cs} & V_{cb} \\ V_{td} & V_{ts} & V_{tb} \end{pmatrix} \begin{pmatrix} d \\ s \\ b \end{pmatrix}, \quad (2.13)$$

where the matrix is the so-called *Cabbibo-Kobayashi-Maskawa (CKM) matrix*, denoted by V_{CKM} .

2.2 Higgs

A pie chart of Higgs decay can be found in Fig. 2.4.

2.3 The physics of proton-proton collisions

The substructure of the proton has been carefully studied in deep inelastic scattering (DIS) experiments at SLAC [16, 17] and DESY [18], which collided electrons or positrons with protons.

In the parton model, *parton distribution functions* (PDFs) describe the probability of finding a parton of type p with momentum fraction x in a collision at some momentum scale Q as a function of the form $f_p(x, Q^2)$ [19–23]. The proton has *valence quarks* and *sea quarks*. To reflect the proton quantum numbers, the PDFs are normalized:

$$\int_0^1 [f_u(x, Q^2) - f_{\bar{u}}(x, Q^2)] dx = 2, \quad \int_0^1 [f_d(x, Q^2) - f_{\bar{d}}(x, Q^2)] dx = 1. \quad (2.14)$$

This follows from the factorization theorem [25, 26], which provides a formula to calculate the cross sections of a hard process with an integral of the form

$$\sigma(pp \rightarrow X + Y) = \sum_{i,j} \int_0^1 \int_0^1 f_i(x_1, Q^2) f_j(x_2, Q^2) \hat{\sigma}_{ij \rightarrow X}(x_1, x_2, Q^2) dx_1 dx_2, \quad (2.15)$$

where $\hat{\sigma}_{ij \rightarrow X}(x_1, x_2, Q^2)$ is the parton-level cross section of the hard process, $i + j \rightarrow X$, and parton i (j) carries a fraction x_1 (x_2) of the momentum of its mother proton.

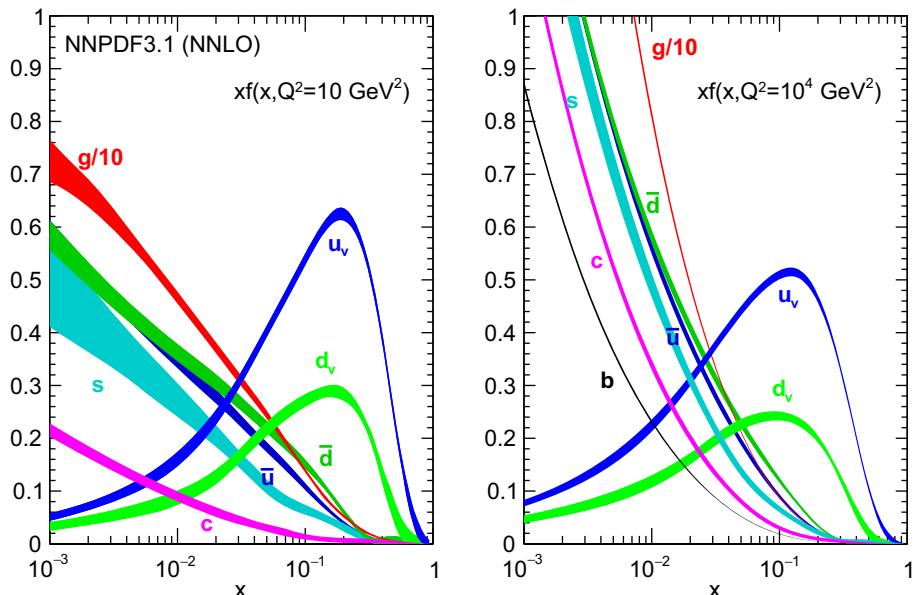


Figure 2.5: Plot of the proton PDF $f_p(x, Q^2)$ times the momentum fraction x as calculated by NNPDF3.1 at NNLO accuracy in perturbation theory for $Q^2 = 10 \text{ GeV}^2$ (left) and $Q^2 = 10^4 \text{ GeV}^2$ (right). Adapted from [24].

¹²⁶ 3 Beyond the Standard Model

¹²⁷ The SM of particle physics is successful. Fine-structure constant $\alpha = e^2/4\pi$ has been precisely
¹²⁸ calculated and measured [27–30]. In 2012, the discovery of the Higgs boson was announced by
¹²⁹ the ATLAS and CMS experiments at the CERN LHC [1–3, 11], more than 47 years after its
¹³⁰ prediction [4, 5]. But there are both problems. The following section highlights several examples
¹³¹ of open questions in physics.

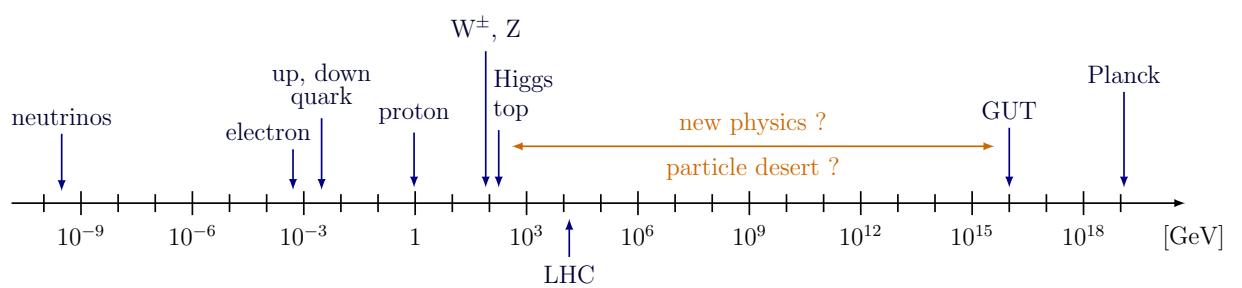


Figure 3.1: Logarithmic scale of different energy scales in particle physics. Adapted from Ref. [9].

4 The CMS Experiment

This chapter will discuss the experimental setup.

4.1 The Large Hadron Collider

The Large Hadron Collider (LHC) is the world's largest and most powerful particle collider with a 27 km circumference and a record collision energy of 13.6 TeV. It surpasses the Tevatron accelerator at Fermilab in the United States [32] (6.3 km, 1.96 TeV), and LEP (209 GeV) [10, Section 32].

During the data-taking period of 2015 to 2018, referred to as "Run 2", the energy of each proton beam was 6.5 TeV, which means the center-of-mass energy was $\sqrt{s} = 13$ TeV. The LHC machine is described in more technical detail in Ref. [33].

4.1.1 Luminosity

It depends on several beam parameters. The simplified expression is [10, p. 533]:

$$\mathcal{L} = \frac{N_1 N_2 f}{A}. \quad (4.1)$$

The LHC is designed to reach the nominal luminosity of $\mathcal{L} = 10^{34} \text{ cm}^{-2} \text{ s}^{-1}$. See Fig. 4.2. Each bunch contains about 110 billion protons [33, 35].

Figure 4.4 shows the distribution of the number of interactions per bunch crossing in all

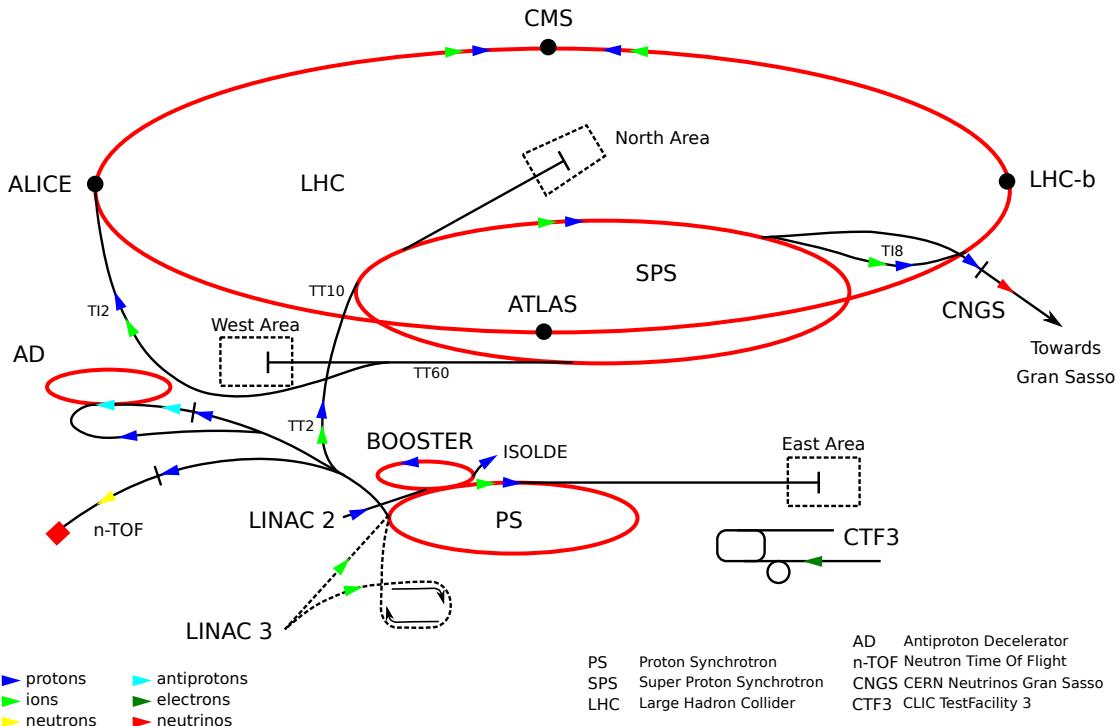


Figure 4.1: CERN's accelerator complex. Taken from [31].

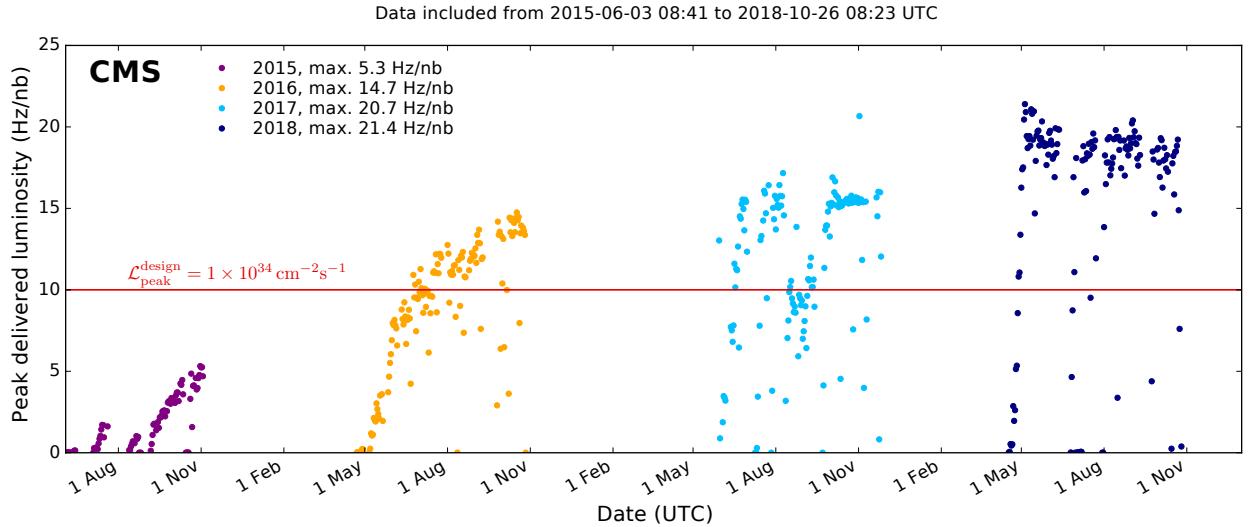


Figure 4.2: The instantaneous luminosity \mathcal{L} . The design luminosity is $\mathcal{L}_{\text{peak}}^{\text{design}} = 10^{34} \text{ cm}^{-2} \text{ s}^{-1}$. Adapted from [34].

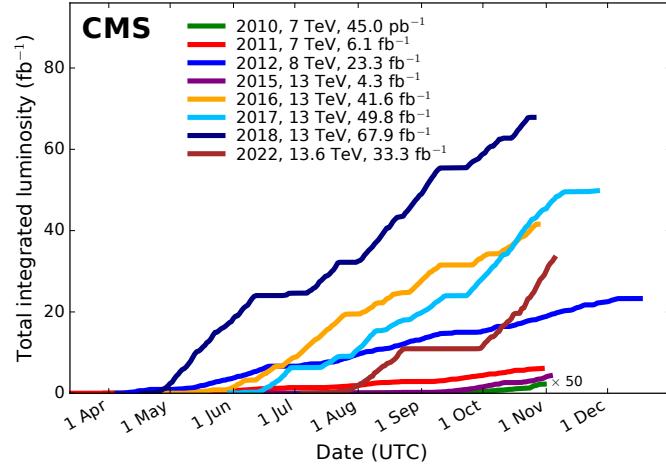


Figure 4.3: Integrated luminosity collected by CMS at $\sqrt{s} = 13 \text{ TeV}$. Figure taken from [34].

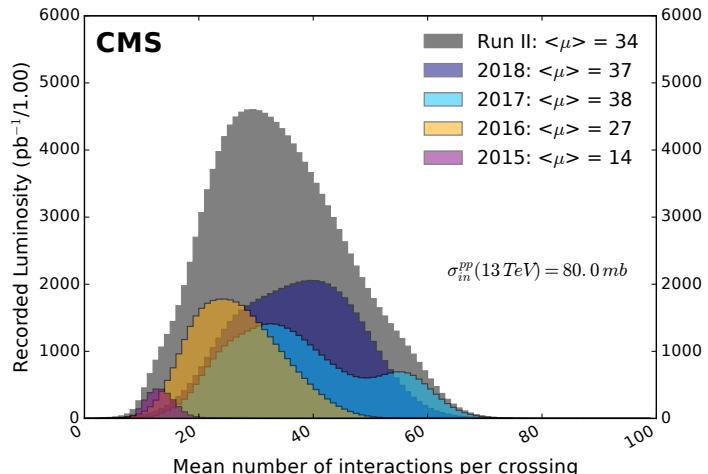


Figure 4.4: Distribution of number of pp interactions, assuming an inelastic cross section of 80 mb. Figure taken from [34].

¹⁴⁷ data-taking years of Run 2.

¹⁴⁸ Figure 4.3 shows the data of each data-taking year with *integrated luminosity* L , which is

$$L := \int_{\text{data taking}} \mathcal{L}(t) dt, \quad (4.2)$$

¹⁴⁹ given in units of inverse area, such as the inverse barn (b^{-1}). Between 2016 and 2018, CMS
¹⁵⁰ collected about 138 fb^{-1} of pp collision data for physics analysis.

¹⁵¹ 4.2 The CMS detector

¹⁵² The Compact Muon Solenoid (CMS) detector at one of the interaction points at the LHC. An
¹⁵³ illustration is shown in Fig. 4.5. A detailed description can be found in Ref. [36].

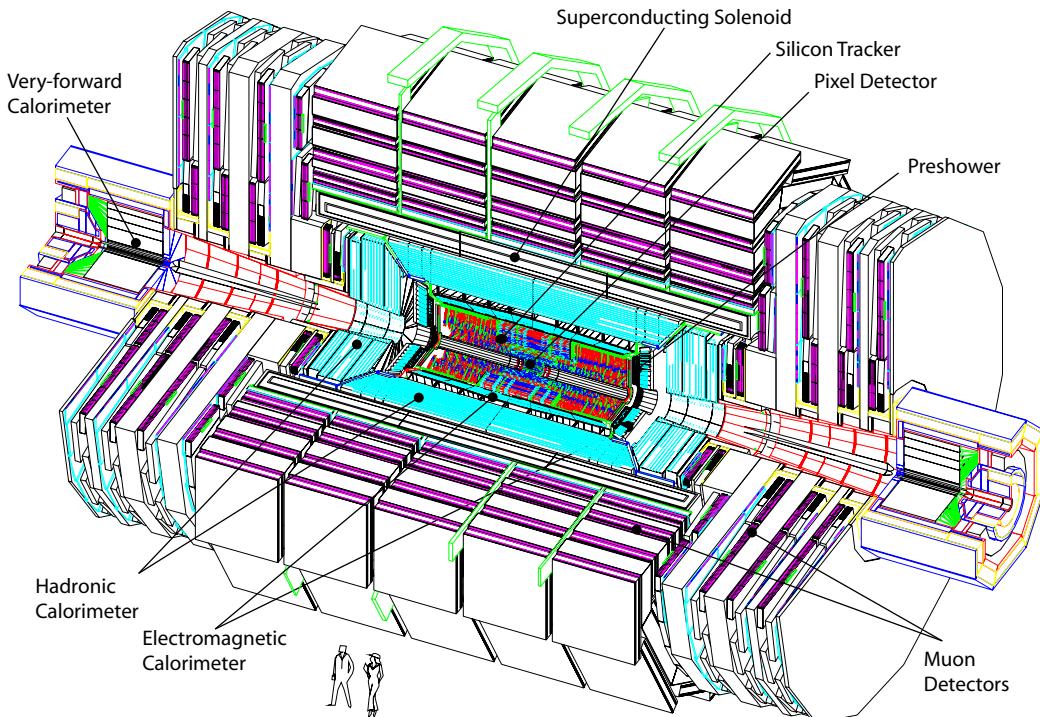


Figure 4.5: The CMS detector. Taken from [36].

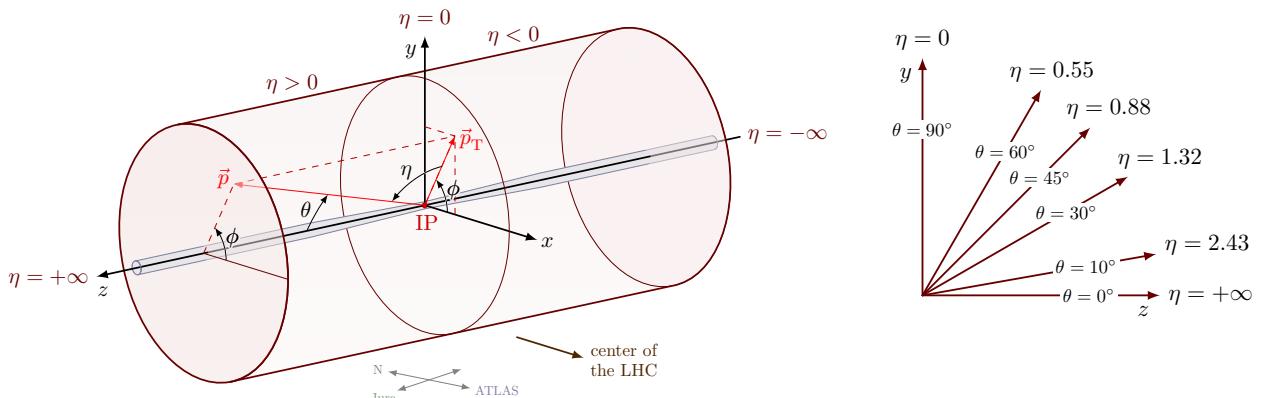


Figure 4.6: **Left:** The conventional coordinate system of CMS with momentum vector \vec{p} . Taken from [37]. **Right:** Pseudorapidity. Taken from [38].

154 **4.2.1 Coordinate system**

155 The conventional coordinate system of CMS is defined in Fig. 4.6.

156 **4.2.2 The solenoid magnet & flux-return yoke**

157 The *superconducting solenoid magnet* is a 13 m long cylinder with an inner diameter of 6 m. The
158 yoke [42].

159 **4.2.3 The pixel tracker**

160 The inner tracker system has a *silicon pixel tracker* and a *silicon microstrip tracker*. Figure 4.8
161 presents a closer look of the full tracker layout. The pixel tracker from 2008 up to 2016 was
162 composed of 1440 sensor modules with a total of 66 million silicon pixels [43]. During the
163 technical shutdown it was upgraded with 1856 modules with 124 million pixels in total [41, 44].
164 Their layouts are compared in Fig. 4.9. See Refs. [43, 45] for more information on the resolution.

165 **4.2.4 The silicon strip tracker**

166 The silicon strip tracker is larger. A detailed description of the tracking and vertexing software
167 is given in Ref. [43].

168 **4.2.5 The electromagnetic calorimeter**

169 The *electromagnetic calorimeter* (ECAL) is built around the tracker. The energy resolution can
170 be parametrized as a function of energy [36]:

$$\left(\frac{\sigma_E}{E}\right)^2 = \left(\frac{S}{\sqrt{E}}\right)^2 \oplus \left(\frac{N}{E}\right)^2 \oplus C^2, \quad (4.3)$$

171 with the stochastic term S , the noise N , and a constant term C . The technical design report [46]
172 describes the ECAL in more technical detail.

173 **4.2.6 The hadronic calorimeter**

174 The last subdetector inside the solenoid is the *hadron calorimeter* (HCAL). The jet energy
175 resolution can be found in Ref. [47]

176 The *very forward HCAL* (HF) is positioned around the beamline outside the detector.

177 **4.2.7 The muon system**

178 The muon system is outside the solenoid magnet. The final momentum resolution can be roughly
179 parametrized as follows:

$$\left(\frac{\sigma_{p_T}}{p_T}\right)^2 = (A \cdot p_T)^2 \oplus C^2, \quad (4.4)$$

180 where A , and C are constants determined by the hit resolution and multiple scattering, respec-
181 tively [48]. The resolution grows with momentum, because the track becomes more straight,
182 which increases the uncertainty in its curvature. The technical design report can be found in
183 Ref. [49].

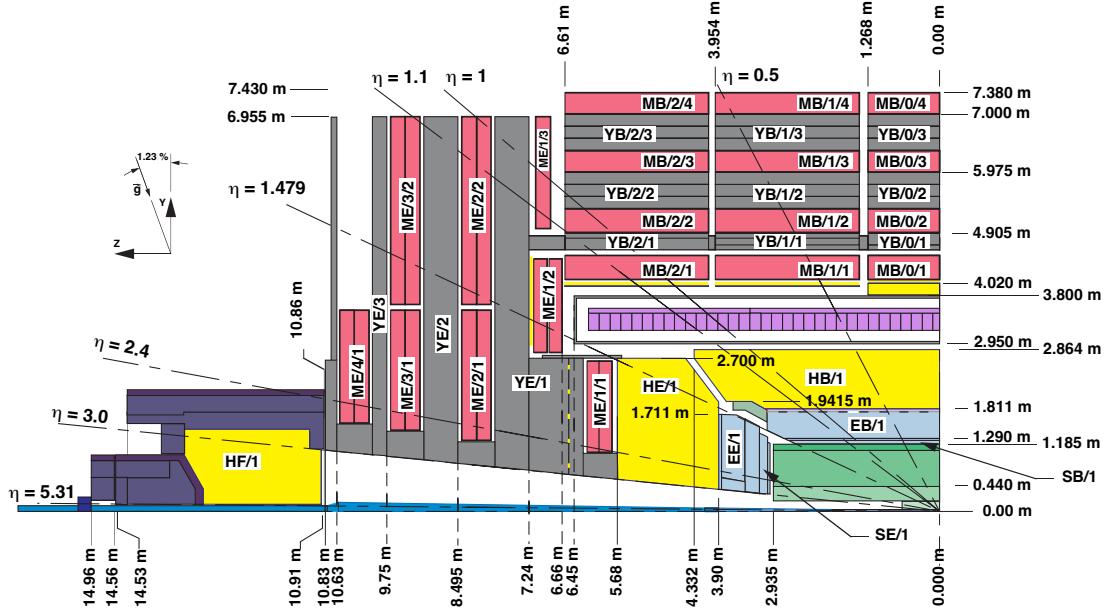


Figure 4.7: Schematic of one quadrant of the CMS detector in the positive zy -plane. Adapted from [39].

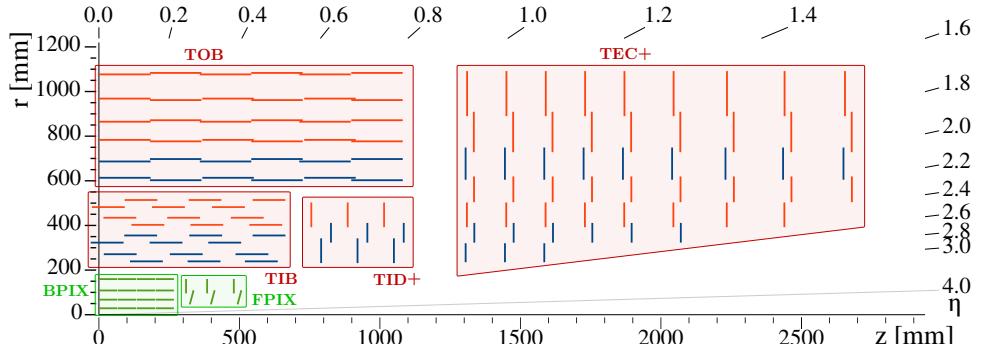


Figure 4.8: Schematic view of the CMS tracking system. Adapted from [40].

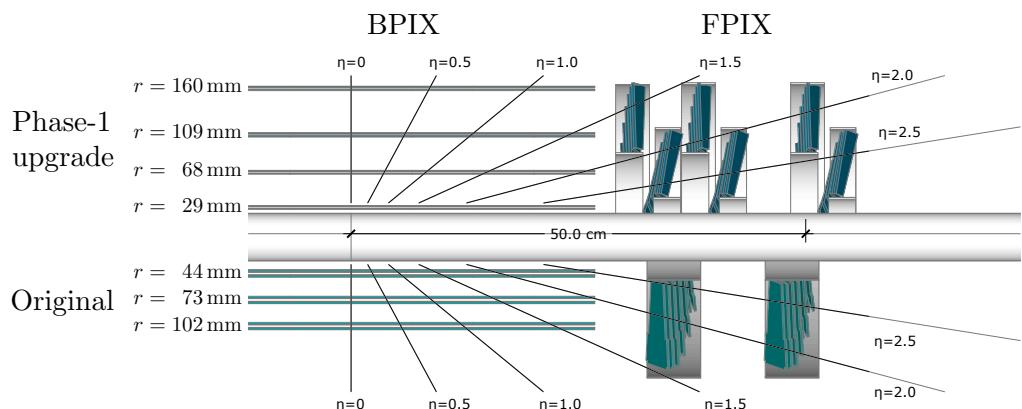


Figure 4.9: Layout of the CMS pixel detector. Adapted from [41].

¹⁸⁴ **4.2.8 The trigger system**

¹⁸⁵ The collision rate of 40 MHz is higher than is possible to record offline. The *L1 trigger* has a
¹⁸⁶ rate of about 100 kHz. The next level, is the *high-level trigger* (HLT). See Ref. [50].

¹⁸⁷ 5 Object & Event Reconstruction

¹⁸⁸ This chapter explains object and event reconstruction in the CMS experiment.

¹⁸⁹ 5.1 Principles of particle identification

¹⁹⁰ Figure 5.1 compares the lifetime, dividing them in different regions of stability in the context of
¹⁹¹ the CMS experiment.

¹⁹² Each of these particles has a unique set of properties that leave a characteristic signal in one
¹⁹³ or more of the subdetector, as illustrated in Fig. 5.2.

¹⁹⁴ 5.2 Particle-flow algorithm

¹⁹⁵ The particle-flow (PF) algorithm [53, 54] fully reconstructs the event of a pp collision with an
¹⁹⁶ optimized combination of all measurements of the CMS subsystems.

¹⁹⁷ Tracks in the inner tracker or muon system are iteratively built from hits, using the *Kalman-*
¹⁹⁸ *filter (KF) technique* [55, 56].

¹⁹⁹ 5.3 Primary vertex

²⁰⁰ The algorithm locates primary vertices (PVs) of pp collisions. The tracks are clustered using the
²⁰¹ *deterministic annealing algorithm* [57]. Finally, candidate vertices are fitted using an *adaptive*
²⁰² *vertex fitter* [58]. The PV with the largest sum of momenta is assumed to be the vertex of the
²⁰³ hard scattering process [43, 54, 59].

²⁰⁴ 5.4 Electrons

²⁰⁵ Electrons are reconstructed by associating a track in the inner tracker to clusters of energy
²⁰⁶ deposits in the ECAL. Candidate tracks are refitted with the *Gaussian sum filter* (GSF) [60].
²⁰⁷ The ECAL clusters are recombined into a so-called *supercluster*. The resolution is documented
²⁰⁸ in Ref. [61, 62].

²⁰⁹ The reconstruction and identification of electrons, as well as high-energy photons, are dis-
²¹⁰ cussed in more detail in Refs. [63] and [61].

²¹¹ The *relative isolation* for electrons is computed with the so-called *rho-effective-area method* [64]:

$$I_{\text{rel}}^e := \frac{\sum_{\text{charged}} p_T + \max(0, \sum_{\text{neutral}} E_T - \rho A_{\text{eff}})}{p_T^e}. \quad (5.1)$$

²¹² 5.5 Muons

²¹³ Muon candidates in CMS are reconstructed as *standalone muons*, *tracker muons*, and/or *global*
²¹⁴ *muons* [65].

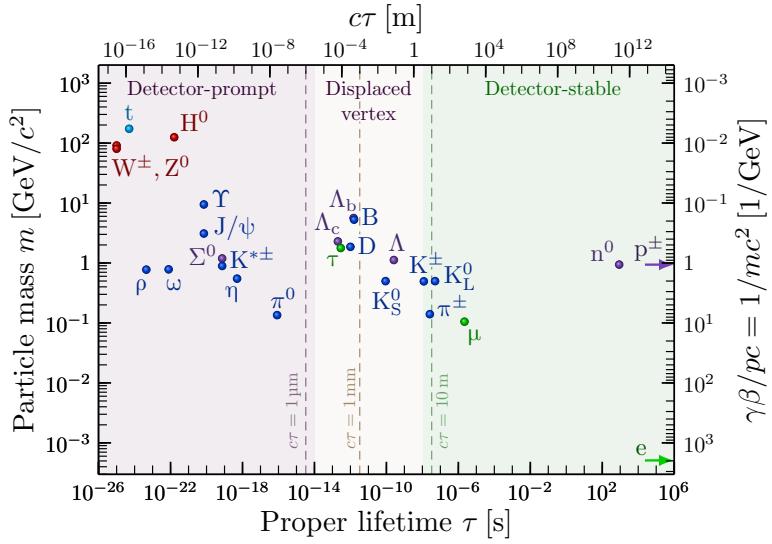


Figure 5.1: Plot of the mass versus lifetime τ of many composite and fundamental SM particles. The decay length is given by $L = \gamma\beta c\tau$, with $\gamma\beta = p/mc$. Adapted from [51].

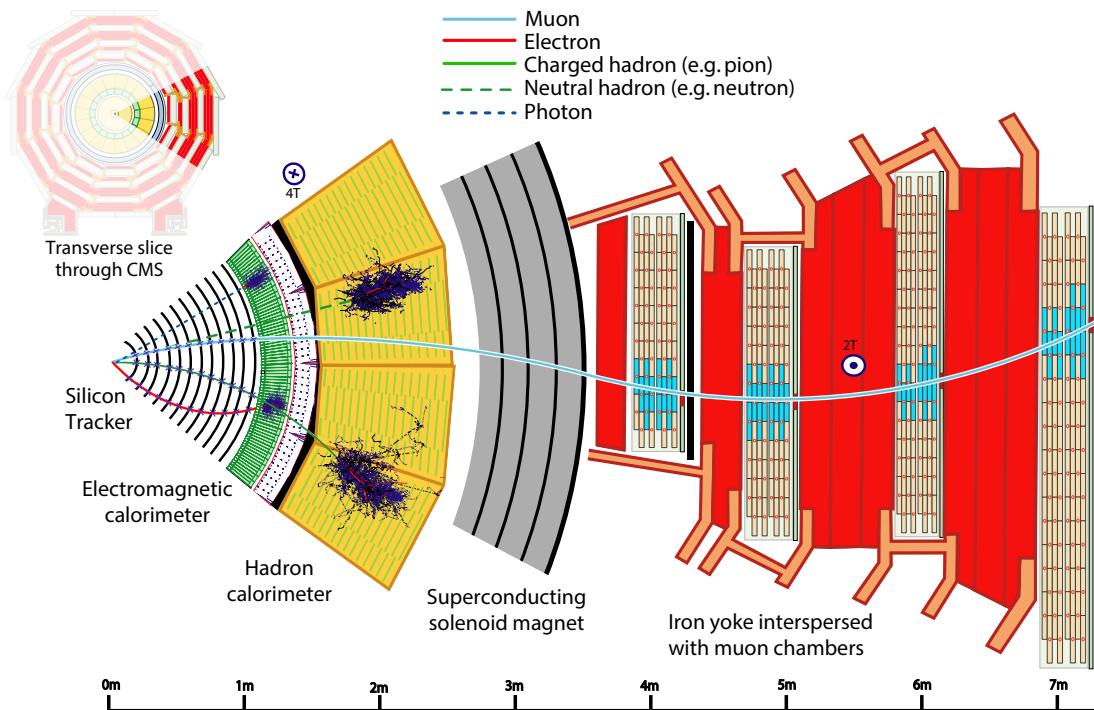


Figure 5.2: Particles in the CMS detector. Adapted from [52].

215 The relative isolation of a muon is defined with the so-called $\Delta\beta$ -*corrections*:

$$I_{\text{rel}}^{\mu} := \frac{\sum_{\text{charged}} p_{\text{T}} + \max(0, \sum_{\text{neutral}} E_{\text{T}} - \Delta\beta \sum_{\text{charged, PU}} p_{\text{T}})}{p_{\text{T}}^{\mu}}. \quad (5.2)$$

216 5.6 Hadronically Decayed τ Leptons

217 Hadronic decays of τ leptons (τ_h) are reconstructed with the *hadron-plus-strips* (HPS) *algorithm* [66–69]. About 65% of hadronic τ decays involve neutral pions, which decay promptly ($\tau = 8.4 \times 10^{-17}$ s) to two photons 98.8% of the time [10, p. 33].

220 The τ_h identification algorithm DEEPTAU [69] was used to discriminate against jets that are 221 initiated by quarks and gluons, as well as electrons and muons, see Fig. 5.5.

222 5.7 Jets

223 Jets are reconstructed with a clustering algorithm. The jet properties must be *infrared safe* and 224 *collinear safe*. The *anti- k_T* (AK) *algorithm* utilizes the metric

$$d_{ij} = \min(p_{\text{T},i}^{-2}, p_{\text{T},j}^{-2}) \frac{\Delta R_{ij}^2}{\Delta R_y^2}, \quad (5.3)$$

225 where $\Delta R_y = \sqrt{\Delta y^2 + \Delta\phi^2}$ is the distance in (y, ϕ) -space with the *rapidity*

$$y := \frac{1}{2} \ln \left(\frac{E + p_z}{E - p_z} \right). \quad (5.4)$$

226 If a cluster i of combined objects satisfies

$$d_{ij} > d_{iB} = p_{\text{T},i}^{-2}, \quad (5.5)$$

227 More info is given in Ref. [54, 71]. The AK algorithm is implemented in the FASTJET library [72, 228 73], and *charged-hadron subtraction* (CHS) is used.

229 The CMS Collaboration determines *jet energy corrections* (JECs) in several steps, which are 230 explained in detail in Ref. [74]. Additionally, the jet energy and *jet energy resolution* (JER) of 231 jets in simulation are corrected to obtain better agreement between simulation and data.

232 Genuine jets are distinguished from pileup jets with the identification algorithm [75]. Identification 233 [76] removes spurious jet-like features that originate from isolated noise patterns in 234 certain HCAL regions.

235 5.8 Bottom quark identification

236 The DEEPCSV algorithm [77, 78] for b tagging jets. DEEPCSV is a deep neural network 237 (DNN) with four hidden layers that is an extension of the combined secondary vertex (CSV) 238 algorithm [77, 78].

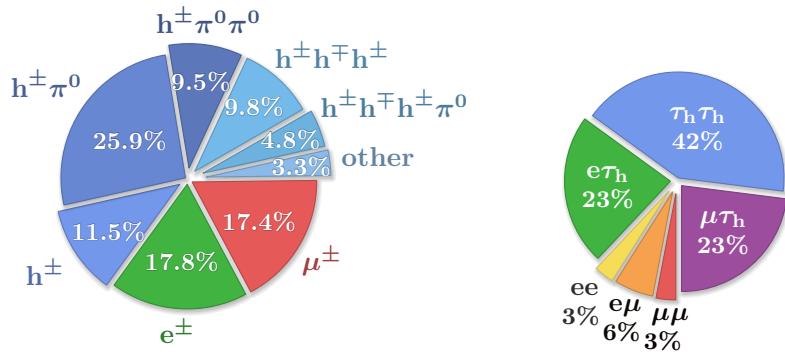


Figure 5.3: Pie charts of branching fractions. **Left:** τ lepton decay. **Right:** Decay channels of a pair of τ leptons. Numbers from PDG [10, p. 28].

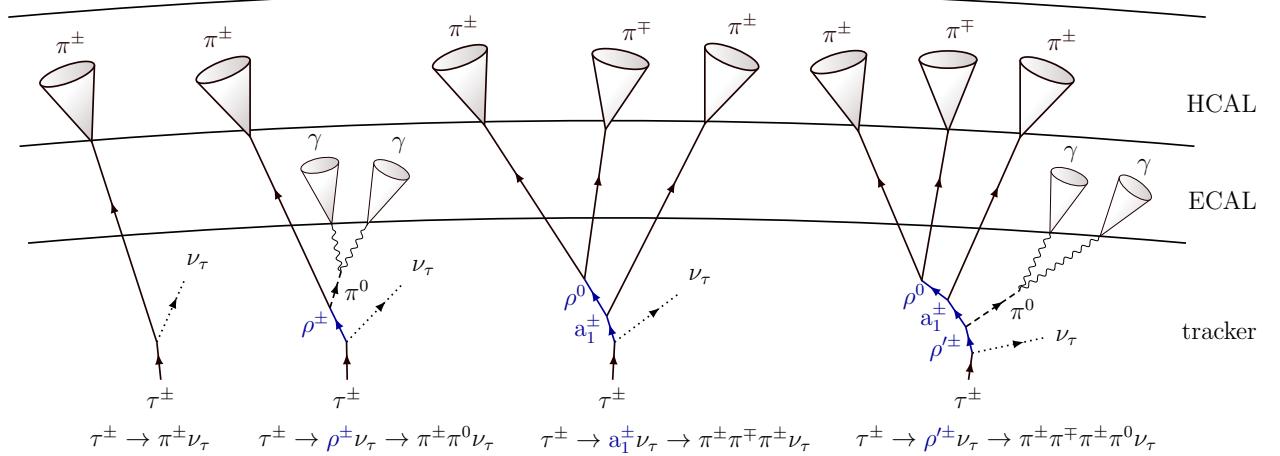


Figure 5.4: An illustration τ_h signatures. Inspired by Ref. [70, p. 37].

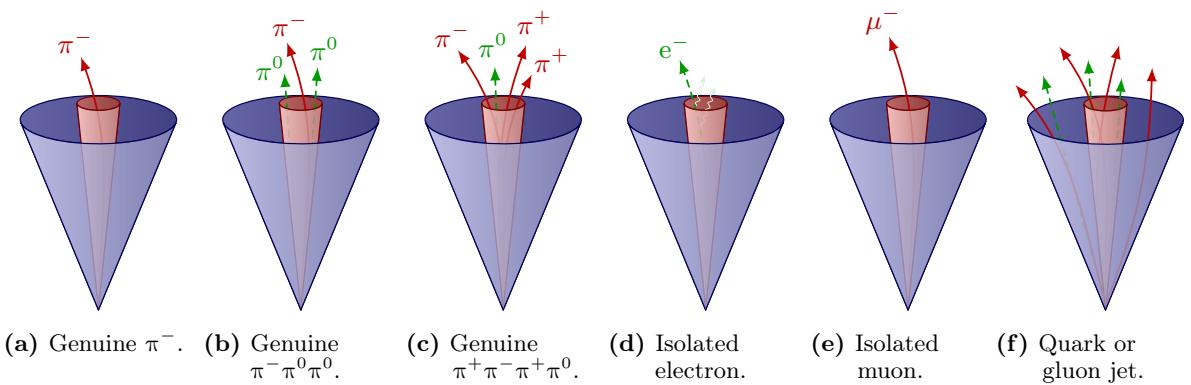
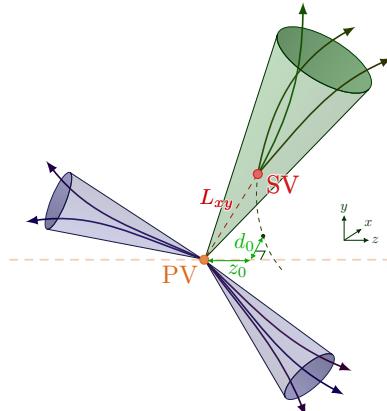
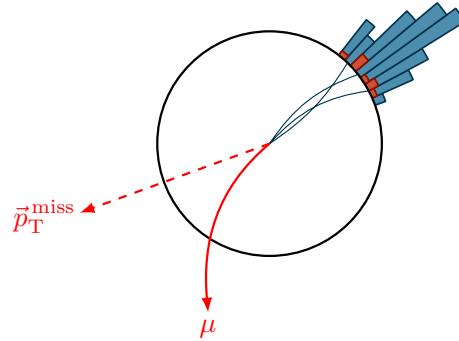


Figure 5.5: Illustration of several hadronic decay modes of the τ leptons (a-c) and their backgrounds (d-f).

**Figure 5.6:** B-tagging.**Figure 5.7:** Illustration of missing transverse energy (MET) with a muon track (red), and energy deposits in the calorimeters.

²³⁹ 5.9 Missing transverse energy

²⁴⁰ The vectorially sum of all particles gives the missing momentum

$$\vec{p}_T^{\text{miss}} = - \sum_i \vec{p}_T^i. \quad (5.6)$$

²⁴¹ This vector, or its length, is often referred to as the *missing transverse momentum*, or *missing*
²⁴² *transverse energy* (MET). Several corrections are applied [54]. More details can be found in
²⁴³ Refs. [79] and [80].

244 **6 Data sets & Simulated Samples**

245 This chapter will discuss in more detail the data sets of pp collision events used, as well as the
246 samples of simulated background events.

247 **6.1 Data sets**

248 The total data set recorded between 2016 and 2018 corresponds to an integrated luminosity of
249 approximately 138 fb^{-1} at $\sqrt{s} = 13 \text{ TeV}$. The run ranges and integrated luminosity per year are
250 listed in Table 6.1.

Table 6.1: LHC run number ranges and integrated luminosity L .

Run number range	$L [\text{fb}^{-1}]$
272007–284044	36.3
297020–306462	41.5
315252–325175	59.7

251 **6.2 Event simulation**

252 The PYTHIA parameters affecting the description of the underlying event are set to the CUETP8M1
253 (CP5) tune for all 2016 (2017 and 2018) samples [82, 83], except for the 2016 $t\bar{t}$ sample, for
254 which CUETP8M2T4 [84] is used. The interaction with the CMS detector is simulated by
255 GEANT4 [85]. Pileup is generated with PYTHIA. Event generation is described in more detail in
256 Refs. [10, p. 717], [86] and [87].

257 **6.3 Backgrounds**

258 **6.3.1 Simulated backgrounds**

259 All the simulated background samples used in this thesis are listed in Table 6.2. The $W + \text{jets}$ and
260 $Z + \text{jets}$ processes are generated with MADGRAPH [88] at LO precision. The MLM jet matching
261 and merging scheme [89] is used to match partons between MADGRAPH and PYTHIA and prevent
262 overcounting. The $Z + \text{jets}$ samples generated at NLO by MADGRAPH5_aMC@NLO [90]. The
263 production of $t\bar{t}$ and singly produced top quarks is simulated with the POWHEG [91–93] 2.0 and
264 1.0 generators, respectively, at NLO precision [94–97]. Diboson production is generated at LO
265 with PYTHIA 8 [98, 99]. The NNPDF3.0 PDF sets [100] are used for 2016. The NNPDF3.1
266 PDF [24] sets are used for 2017 and 2018 samples.

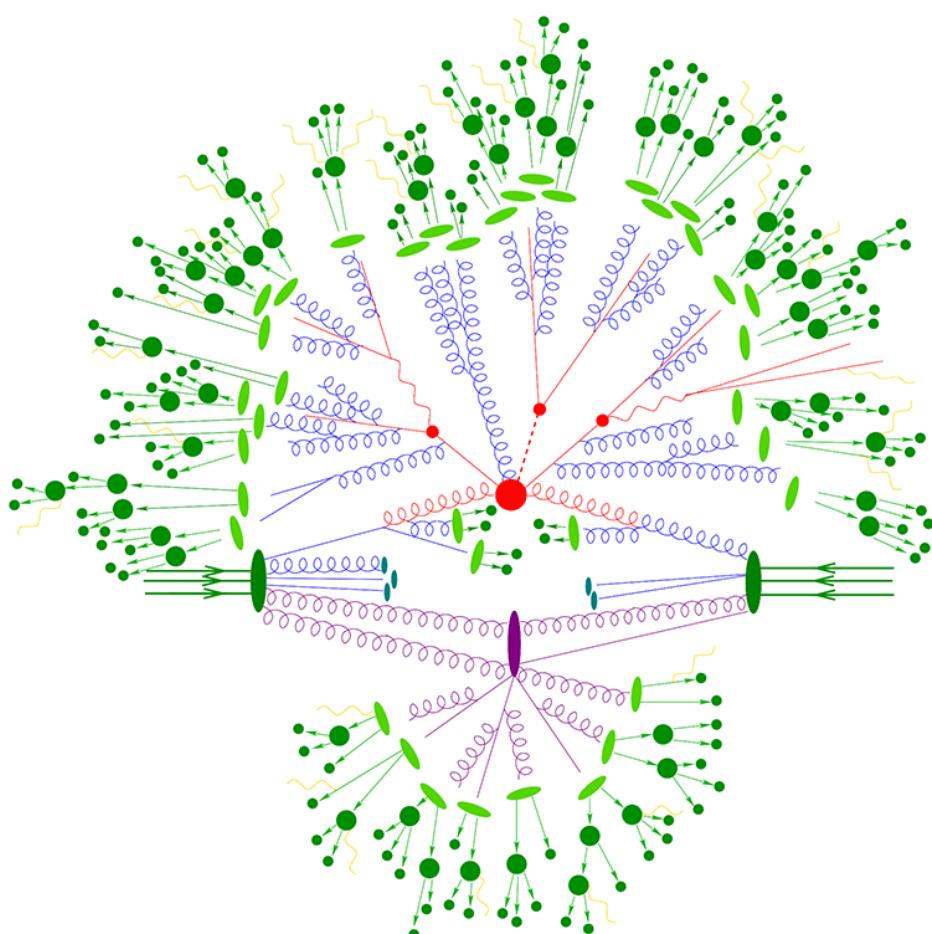


Figure 6.1: Schematic diagram explaining event generation of two colliding protons. Retrieved from [81].

Table 6.2: Summary of simulated SM backgrounds

Process	Generators	Cross section σ [pb]
Drell-Yan, $Z/\gamma^* \rightarrow \ell^+\ell^-$, LO		
+ jets, $10 < m_{\ell\ell} < 50$ GeV	MADGRAPH, PYTHIA	15810.0 (LO), 18610.0 (NLO)
+ jets, $m_{\ell\ell} > 50$ GeV	MADGRAPH, PYTHIA	5343.0 (LO), 6077.2 (NNLO)
+ 1 jets, $m_{\ell\ell} > 50$ GeV	MADGRAPH, PYTHIA	877.8 (LO)
+ 2 jets, $m_{\ell\ell} > 50$ GeV	MADGRAPH, PYTHIA	304.4 (LO)
+ 3 jets, $m_{\ell\ell} > 50$ GeV	MADGRAPH, PYTHIA	111.5 (LO)
+ 4 jets, $m_{\ell\ell} > 50$ GeV	MADGRAPH, PYTHIA	44.05 (LO)
Drell-Yan, $Z/\gamma^* \rightarrow \ell^+\ell^-$, NLO		
+ jets, $m_{\ell\ell} \in [100, 200]$ GeV	aMC@NLO, PYTHIA	247.8 (NLO)
+ jets, $m_{\ell\ell} \in [200, 400]$ GeV	aMC@NLO, PYTHIA	8.502 (NLO)
+ jets, $m_{\ell\ell} \in [400, 500]$ GeV	aMC@NLO, PYTHIA	0.4514 (NLO)
+ jets, $m_{\ell\ell} \in [500, 700]$ GeV	aMC@NLO, PYTHIA	0.2558 (NLO)
+ jets, $m_{\ell\ell} \in [700, 800]$ GeV	aMC@NLO, PYTHIA	0.04023 (NLO)
+ jets, $m_{\ell\ell} \in [800, 1000]$ GeV	aMC@NLO, PYTHIA	0.03406 (NLO)
+ jets, $m_{\ell\ell} \in [1000, 1500]$ GeV	aMC@NLO, PYTHIA	0.01828 (NLO)
+ jets, $m_{\ell\ell} \in [1500, 2000]$ GeV	aMC@NLO, PYTHIA	0.002367 (NLO)
+ jets, $m_{\ell\ell} \in [2000, 3000]$ GeV	aMC@NLO, PYTHIA	5.409×10^{-4} (NLO)
+ jets, $m_{\ell\ell} \in [3000, \infty]$ GeV	aMC@NLO, PYTHIA	3.048×10^{-5} (NLO)
W + jets, $W \rightarrow \ell\nu$		
+ jets	MADGRAPH, PYTHIA	52940.0 (LO), 61526.7 (NLO)
+ 1 jets	MADGRAPH, PYTHIA	8104.0 (LO)
+ 2 jets	MADGRAPH, PYTHIA	2793.0 (LO)
+ 3 jets	MADGRAPH, PYTHIA	992.5 (LO)
+ 4 jets	MADGRAPH, PYTHIA	544.3 (LO)
t̄t + jets		833.9 (NNLO)
Fully leptonic	POWHEG, PYTHIA	88.29 (NNLO), $\mathcal{B} = 10.6\%$
Semi-leptonic	POWHEG, PYTHIA	365.35 (NNLO), $\mathcal{B} = 43.9\%$
Fully Hadronic	POWHEG, PYTHIA	377.96 (NNLO), $\mathcal{B} = 45.4\%$
Single top		
t + W ⁻	POWHEG, PYTHIA	35.85 (NNLO)
t̄ + W ⁺	POWHEG, PYTHIA	35.85 (NNLO)
Single t, t channel	POWHEG, PYTHIA	136.02 (NNLO)
Single t̄, t channel	POWHEG, PYTHIA	80.95 (NNLO)
Diboson		
WW	PYTHIA	75.88 (LO)
WZ	PYTHIA	27.60 (LO)
ZZ	PYTHIA	12.14 (LO)

6.3.2 Cross sections

Table 6.2 also lists the theoretical cross sections σ for each sample. The events are weighted by

$$Z = \frac{L\sigma}{N_{\text{tot}}}, \quad (6.1)$$

or with generator weight w_{gen} ,

$$Z = \frac{L\sigma}{\sum w_{\text{gen}}} w_{\text{gen}}. \quad (6.2)$$

The LO cross sections of the Z + jets and W + jets samples in Table 6.2 are computed with MADGRAPH. The Z + jets cross section is computed with FEWZ [101] program at NNLO in perturbative QCD, and with NLO electroweak corrections. The t \bar{t} +jets cross section was computed with the TOP++v2.0 program [102, 103] at NNLO and at next-to-next-to-leading logarithmic (NNLL) accuracy. The W + jets production is normalized with cross sections computed at NLO accuracy.

²⁷⁶ 7 Event Selection

²⁷⁷ This chapter will discuss in more detail the data sets of pp collision events used, as well as the
²⁷⁸ samples of simulated background events.

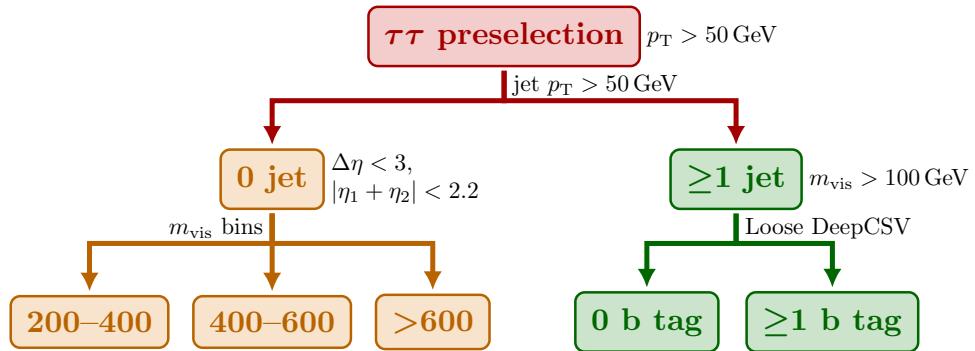


Figure 7.1: Flow chart of event selection.

279 References

- 280 [1] CMS Collaboration, “Observation of a new boson at a mass of 125 GeV with the CMS
281 experiment at the LHC”, *Phys. Lett. B* **716** (2012) 30,
282 doi:10.1016/j.physletb.2012.08.021, arXiv:1207.7235.
- 283 [2] ATLAS Collaboration, “Observation of a new particle in the search for the Standard
284 Model Higgs boson with the ATLAS detector at the LHC”, *Phys. Lett. B* **716** (2012) 1,
285 doi:10.1016/j.physletb.2012.08.020, arXiv:1207.7214.
- 286 [3] CMS Collaboration, “Observation of a new boson with mass near 125 GeV in pp
287 collisions at $\sqrt{s} = 7$ and 8 TeV”, *JHEP* **06** (2013) 081, doi:10.1007/JHEP06(2013)081,
288 arXiv:1303.4571.
- 289 [4] F. Englert and R. Brout, “Broken Symmetry and the Mass of Gauge Vector Mesons”,
290 *Phys. Rev. Lett.* **13** (1964) 321, doi:10.1103/PhysRevLett.13.321.
- 291 [5] P. W. Higgs, “Broken Symmetries and the Masses of Gauge Bosons”, *Phys. Rev. Lett.* **13**
292 (1964) 508, doi:10.1103/PhysRevLett.13.508.
- 293 [6] L. M. Brown, M. Dresden, L. H. Hoddeson, and M. West, eds., “Proceedings, 2nd
294 International Symposium on on the History of Particle Physics in the 1950s: Pions to
295 Quarks: Batavia, USA, May 1-4, 1985”. Univ. Pr., Cambridge, UK, (1989).
- 296 [7] L. H. Hoddeson, L. Brown, M. Riordan, and M. Dresden, eds., “The Rise of the standard
297 model: Particle physics in the 1960s and 1970s. Proceedings, Conference, Stanford, USA,
298 June 24-27, 1992”. (1997).
- 299 [8] D. Griffiths, “Introduction to Elementary Particles”. Wiley-VCH, 2 edition, 2008.
300 ISBN 978-3-527-40601-2.
- 301 [9] Neutelings, Izaak, “History timeline and energy scales – TikZ.net”,
302 <https://tikz.net/timeline/>, 2022. (Retrieved March 26, 2022).
- 303 [10] Particle Data Group, “Review of Particle Physics”, *PTEP* **2022** (2022) 083C01,
304 doi:10.1093/ptep/ptac097.
- 305 [11] ATLAS and CMS Collaborations, “Combined Measurement of the Higgs Boson Mass in
306 pp Collisions at $\sqrt{s} = 7$ and 8 TeV with the ATLAS and CMS Experiments”, *Phys. Rev.*
307 *Lett.* **114** (2015) 114, doi:10.1103/PhysRevLett.114.191803, arXiv:1503.07589.
- 308 [12] A. Ferrari and N. Rompotis, “Exploration of Extended Higgs Sectors with Run-2
309 Proton–Proton Collision Data at the LHC”, *Symmetry* **13** (2021), no. 11, 2144,
310 doi:10.3390/sym14081546. [Erratum: Symmetry 14, 1546 (2022)].
- 311 [13] Wikimedia Commons, “File:Standard Model of Elementary Particles.svg — Wikimedia
312 Commons, the free media repository”, <https://commons.wikimedia.org/wiki/File:>
313 *Standard_Model_of_Elementary_Particles.svg*, 2023. (Retrieved Jan 13, 2023).
- 314 [14] G. Isidori, “Lectures notes on Flavour physics”,

- 315 <https://www.physik.uzh.ch/en/groups/isidori/teaching.html>, 2016. (Retrieved
316 Nov 16, 2022).
- 317 [15] S. L. Glashow, J. Iliopoulos, and L. Maiani, “Weak Interactions with Lepton-Hadron
318 Symmetry”, *Phys. Rev. D* **2** (1970) 1285, doi:10.1103/PhysRevD.2.1285.
- 319 [16] E. D. Bloom et al., “High-Energy Inelastic e^-p Scattering at 6° and 10° ”, *Phys. Rev.*
320 *Lett.* **23** (1969) 930, doi:10.1103/PhysRevLett.23.930.
- 321 [17] M. Breidenbach et al., “Observed Behavior of Highly Inelastic Electron-Proton
322 Scattering”, *Phys. Rev. Lett.* **23** (1969) 935, doi:10.1103/PhysRevLett.23.935.
- 323 [18] **ZEUS** and **H1** Collaborations, “Combination of measurements of inclusive deep inelastic
324 $e^\pm p$ scattering cross sections and QCD analysis of HERA data”, *Eur. Phys. J. C* **75**
325 (2015), no. 12, 580, doi:10.1140/epjc/s10052-015-3710-4, arXiv:1506.06042.
- 326 [19] R. P. Feynman, “The Behavior of Hadron Collisions at Extreme Energies”, in *High*
327 *Energy Collisions: Third International Conference*, p. 237. Stony Brook, N.Y., U.S.A.,
328 1969.
- 329 [20] J. D. Bjorken and E. A. Paschos, “Inelastic Electron-Proton and γ -Proton Scattering and
330 the Structure of the Nucleon”, *Phys. Rev.* **185** (1969) 1975,
331 doi:10.1103/PhysRev.185.1975.
- 332 [21] J. M. Campbell, J. W. Huston, and W. J. Stirling, “Hard Interactions of Quarks and
333 Gluons: A Primer for LHC Physics”, *Rept. Prog. Phys.* **70** (2007) 89,
334 doi:10.1088/0034-4885/70/1/R02, arXiv:hep-ph/0611148.
- 335 [22] R. Placakyte, “Parton Distribution Functions”, in *Proceedings, 31st International*
336 *Conference on Physics in collisions (PIC 2011)*. Vancouver, Canada, 2011.
337 arXiv:1111.5452.
- 338 [23] **ALICE** Collaboration, “Parton distributions for the LHC”, *Eur. Phys. J. C* **63** (2009)
339 189, doi:10.1140/epjc/s10052-009-1072-5, arXiv:0901.0002.
- 340 [24] **NNPDF** Collaboration, “Parton distributions from high-precision collider data”, *Eur.*
341 *Phys. J. C* **77** (2017), no. 10, 663, doi:10.1140/epjc/s10052-017-5199-5,
342 arXiv:1706.00428.
- 343 [25] J. C. Collins and D. E. Soper, “The Theorems of Perturbative QCD”, *Ann. Rev. Nucl.*
344 *Part. Sci.* **37** (1987) 383, doi:10.1146/annurev.ns.37.120187.002123.
- 345 [26] J. C. Collins, D. E. Soper, and G. F. Sterman, “Factorization of Hard Processes in
346 QCD”, *Adv. Ser. Direct. High Energy Phys.* **5** (1989) 11,
347 doi:10.1142/9789814503266_0001, arXiv:hep-ph/0409313.
- 348 [27] T. Aoyama, M. Hayakawa, T. Kinoshita, and M. Nio, “Tenth-Order QED Contribution
349 to the Electron g-2 and an Improved Value of the Fine Structure Constant”, *Phys. Rev.*
350 *Lett.* **109** (2012) 111807, doi:10.1103/PhysRevLett.109.111807, arXiv:1205.5368.
- 351 [28] T. Aoyama, M. Hayakawa, T. Kinoshita, and M. Nio, “Tenth-Order Electron Anomalous
352 Magnetic Moment — Contribution of Diagrams without Closed Lepton Loops”, *Phys.*
353 *Rev. D* **91** (2015), no. 3, 033006,
354 doi:10.1103/PhysRevD.91.033006, 10.1103/PhysRevD.96.019901, arXiv:1412.8284.
355 [Erratum: *Phys. Rev. D* **96**, no. 1, 019901 (2017)].

- 356 [29] M. Nio, “QED tenth-order contribution to the electron anomalous magnetic moment and
357 a new value of the fine-structure constant”, Fundamental Constants Meeting, Eltville,
358 Germany, 2015. <http://www.bipm.org/cc/CODATA-TGFC/Allowed/2015-02/Nio.pdf>.
- 359 [30] D. Hanneke, S. Fogwell, and G. Gabrielse, “New Measurement of the Electron Magnetic
360 Moment and the Fine Structure Constant”, *Phys. Rev. Lett.* **100** (2008) 120801,
361 doi:10.1103/PhysRevLett.100.120801, arXiv:0801.1134.
- 362 [31] L. Forthomme (Wikimedia Commons), “File:Cern-accelerator-complex.svg — Wikimedia
363 Commons, the free media repository”,
364 <https://commons.wikimedia.org/wiki/File:Cern-accelerator-complex.svg>, 2016.
365 (Retrieved Jul 24, 2017).
- 366 [32] S. Holmes, R. S. Moore, and V. Shiltsev, “Overview of the Tevatron Collider Complex:
367 Goals, Operations and Performance”, *JINST* **6** (2011) T08001,
368 doi:10.1088/1748-0221/6/08/T08001, arXiv:1106.0909.
- 369 [33] L. Evans and P. Bryant, “LHC Machine”, *JINST* **3** (2008), no. 08, S08001,
370 doi:10.1088/1748-0221/3/08/S08001.
- 371 [34] CMS Collaboration, “Public CMS Luminosity Information”.
372 <https://twiki.cern.ch/twiki/bin/view/CMSPublic/LumiPublicResults>. (Retrieved
373 Dec 6, 2022).
- 374 [35] I. Efthymiopoulos et al., “Bunch Luminosity Variations in LHC Run 2. BUNCH
375 LUMINOSITY VARIATIONS IN LHC RUN 2”, *JACoW IPAC* **2021** (2021) 4094,
376 doi:10.18429/JACoW-IPAC2021-THPAB172.
- 377 [36] CMS Collaboration, “The CMS experiment at the CERN LHC”, *JINST* **3** (2008)
378 S08004, doi:10.1088/1748-0221/3/08/S08004.
- 379 [37] Neutelings, Izaak, “CMS coordinate system – TikZ.net”,
380 https://tikz.net/axis3d_cms/, 2022. (Retrieved Dec 2, 2022).
- 381 [38] Neutelings, Izaak, “Pseudorapidity – TikZ.net”,
382 https://tikz.net/axis2d_pseudorapidity/, 2022. (Retrieved Dec 2, 2022).
- 383 [39] CMS Collaboration, “Performance of the CMS Drift Tube Chambers with Cosmic Rays”,
384 *JINST* **5** (2010) T03015, doi:10.1088/1748-0221/5/03/T03015, arXiv:0911.4855.
- 385 [40] CMS Collaboration, “CMS Tracker Detector Performance Results”,
386 <https://twiki.cern.ch/twiki/bin/view/CMSPublic/DPGResultsTRK>, 2022.
387 (Retrieved Dec 2, 2022).
- 388 [41] CMS Tracker Group, “The CMS Phase-1 Pixel Detector Upgrade”, *JINST* **16** (2021),
389 no. 02, P02027, doi:10.1088/1748-0221/16/02/P02027, arXiv:2012.14304.
- 390 [42] CMS Collaboration, “Precise Mapping of the Magnetic Field in the CMS Barrel Yoke
391 using Cosmic Rays”, *JINST* **5** (2015) T03021, doi:10.1088/1748-0221/5/03/T03021,
392 arXiv:0910.5530.
- 393 [43] CMS Collaboration, “Description and performance of track and primary-vertex
394 reconstruction with the CMS tracker”, *JINST* **9** (2014) P10009,
395 doi:10.1088/1748-0221/9/10/P10009, arXiv:1405.6569.

- 396 [44] CMS Collaboration, “The Phase-1 upgrade of the CMS pixel detector”, *JINST* **12**
397 (2017), no. 07, C07009, doi:10.1088/1748-0221/12/07/C07009.
- 398 [45] CMS Collaboration, “CMS Tracking POG Performance Plots For 2017 with PhaseI
399 pixel detector”, [https://twiki.cern.ch/twiki/bin/view/CMSPublic/
400 TrackingPOGPerformance2017MC#Vertex_Resolutions](https://twiki.cern.ch/twiki/bin/view/CMSPublic/TrackingPOGPerformance2017MC#Vertex_Resolutions), 2022. (Retrieved Dec 8, 2022).
- 401 [46] CMS Collaboration, “The CMS electromagnetic calorimeter project: Technical Design
402 Report”, Technical Design Report CMS. CERN, Geneva, 1997.
- 403 [47] CMS Collaboration, “Jet energy scale and resolution in the CMS experiment in pp
404 collisions at 8 TeV”, *JINST* **12** (2017), no. 02, P02014,
405 doi:10.1088/1748-0221/12/02/P02014, arXiv:1607.03663.
- 406 [48] E. Manca, “Validation of the muon momentum resolution in view of the W mass
407 measurement with the CMS experiment”. PhD thesis, INFN, Pisa, 2016.
408 CMS-TS-2016-024, CERN-THESIS-2016-173.
- 409 [49] CMS Collaboration, “The CMS muon project : Technical Design Report”, Technical
410 Design Report CMS. CERN, Geneva, 1997.
- 411 [50] CMS Collaboration, “The CMS trigger system”, *JINST* **12** (2017) P01020,
412 doi:10.1088/1748-0221/12/01/P01020, arXiv:1609.02366.
- 413 [51] L. Lee, C. Ohm, A. Soffer, and T.-T. Yu, “Collider Searches for Long-Lived Particles
414 Beyond the Standard Model”, *Prog. Part. Nucl. Phys.* **106** (2019) 210,
415 doi:10.1016/j.ppnp.2019.02.006, arXiv:1810.12602. [Erratum:
416 Prog.Part.Nucl.Phys. 122, 103912 (2022)].
- 417 [52] D. Barney, “CMS Slice”, <https://cds.cern.ch/record/2628641/>, 2015. (Retrieved
418 Dec 8, 2022).
- 419 [53] CMS Collaboration, “Commissioning of the Particle-flow Event Reconstruction with the
420 first LHC collisions recorded in the CMS detector”, CMS Physics Analysis Summary
421 CMS-PAS-PFT-10-001, CERN, 2010.
- 422 [54] CMS Collaboration, “Particle-flow reconstruction and global event description with the
423 CMS detector”, *JINST* **12** (2017) P10003, doi:10.1088/1748-0221/12/10/P10003,
424 arXiv:1706.04965.
- 425 [55] W. Adam, B. Mangano, T. Speer, and T. Todorov, “Track Reconstruction in the CMS
426 tracker”, technical report, CERN, Geneva, 2006.
- 427 [56] R. Frühwirth, “Application of Kalman filtering to track and vertex fitting”, *Nucl.
428 Instrum. Meth. A* **262** (1987) 444, doi:10.1016/0168-9002(87)90887-4.
- 429 [57] K. Rose, “Deterministic annealing for clustering, compression, classification, regression,
430 and related optimization problems”, *IEEE Proc.* **86** (1998), no. 11, 2210,
431 doi:10.1109/5.726788.
- 432 [58] R. Frühwirth, W. Waltenberger, and P. Vanlaer, “Adaptive Vertex Fitting”, technical
433 report, CERN, Geneva, 2007.
- 434 [59] CMS Collaboration, “Technical proposal for the Phase-II upgrade of the Compact Muon
435 Solenoid”, CMS Technical Proposal CERN-LHCC-2015-010, CMS-TDR-15-02, CERN,

- 436 2015.
- 437 [60] W. Adam, R. Frühwirth, A. Strandlie, and T. Todorov, “Reconstruction of electrons with
438 the Gaussian-sum filter in the CMS tracker at the LHC”, *Journal of Physics G: Nuclear
439 and Particle Physics* **31** (2005), no. 9, N9, doi:10.1088/0954-3899/31/9/n01.
- 440 [61] **CMS** Collaboration, “Electron and photon reconstruction and identification with the
441 CMS experiment at the CERN LHC”, *JINST* **16** (2021) P05014,
442 doi:10.1088/1748-0221/16/05/P05014, arXiv:2012.06888.
- 443 [62] **CMS** Collaboration, “ECAL 2016 refined calibration and Run2 summary plots”, CMS
444 Detector Performance Summary CMS-DP-2020-021, CERN, 2020.
- 445 [63] **CMS** Collaboration, “Performance of electron reconstruction and selection with the
446 CMS detector in proton-proton collisions at $\sqrt{s} = 8$ TeV”, *JINST* **10** (2015) P06005,
447 doi:10.1088/1748-0221/10/06/P06005, arXiv:1502.02701.
- 448 [64] M. Cacciari and G. P. Salam, “Pileup subtraction using jet areas”, *Phys. Lett. B* **659**
449 (2008) 119, doi:10.1016/j.physletb.2007.09.077, arXiv:0707.1378.
- 450 [65] **CMS** Collaboration, “Performance of the CMS muon detector and muon reconstruction
451 with proton-proton collisions at $\sqrt{s} = 13$ TeV”, *JINST* **13** (2018) P06015,
452 doi:10.1088/1748-0221/13/06/P06015, arXiv:1804.04528.
- 453 [66] **CMS** Collaboration, “Performance of τ -lepton reconstruction and identification in
454 CMS”, *JINST* **7** (2012), no. 01, P01001, doi:10.1088/1748-0221/7/01/P01001,
455 arXiv:1109.6034.
- 456 [67] **CMS** Collaboration, “Performance of reconstruction and identification of τ leptons
457 decaying to hadrons and ν_τ in pp collisions at $\sqrt{s} = 13$ TeV”, *JINST* **13** (2018) P10005,
458 doi:10.1088/1748-0221/13/10/P10005, arXiv:1809.02816.
- 459 [68] **CMS** Collaboration, “Performance of reconstruction and identification of tau leptons in
460 their decays to hadrons and tau neutrino in LHC Run-2”, CMS Physics Analysis
461 Summary CMS-PAS-TAU-16-002, CERN, 2016.
- 462 [69] **CMS** Collaboration, “Identification of hadronic tau lepton decays using a deep neural
463 network”, *JINST* **17** (2022), no. 07, P07023, doi:10.1088/1748-0221/17/07/p07023,
464 arXiv:2201.08458.
- 465 [70] Y. Takahashi and M. Tomoto, “Measurement of the top-quark pair production
466 cross-section in pp collisions at $\sqrt{s} = 7$ TeV using final states with an electron or a muon
467 and a hadronically decaying τ -lepton”. PhD thesis, Nagoya University, 2012.
468 CERN-THESIS-2012-252.
- 469 [71] M. Cacciari, G. P. Salam, and G. Soyez, “The anti- k_t jet clustering algorithm”, *JHEP*
470 **04** (2008) 063, doi:10.1088/1126-6708/2008/04/063, arXiv:0802.1189.
- 471 [72] M. Cacciari and G. P. Salam, “Dispelling the N^3 myth for the k_T jet-finder”, *Phys. Lett. B* **641**
472 (2006) 57, doi:10.1016/j.physletb.2006.08.037, arXiv:hep-ph/0512210.
- 473 [73] M. Cacciari, G. P. Salam, and G. Soyez, “FastJet user manual”, *Eur. Phys. J. C* **72**
474 (2012) 1896, doi:10.1140/epjc/s10052-012-1896-2, arXiv:1111.6097.
- 475 [74] **CMS** Collaboration, “Determination of jet energy calibration and transverse momentum

- 476 resolution in CMS”, *JINST* **6** (2011) P11002, doi:10.1088/1748-0221/6/11/P11002,
477 arXiv:1107.4277.
- 478 [75] **CMS** Collaboration, “Pileup Jet Identification”, CMS Physics Analysis Summary
479 CMS-PAS-JME-13-005, CERN, 2013.
- 480 [76] **CMS** Collaboration, “Jet algorithms performance in 13 TeV data”, CMS Physics
481 Analysis Summary CMS-PAS-JME-16-003, CERN, 2017.
- 482 [77] D. Guest et al., “Jet Flavor Classification in High-Energy Physics with Deep Neural
483 Networks”, *Phys. Rev. D* **94** (2016), no. 11, 112002,
484 doi:10.1103/PhysRevD.94.112002, arXiv:1607.08633.
- 485 [78] **CMS** Collaboration, “Identification of heavy-flavour jets with the CMS detector in pp
486 collisions at 13 TeV”, *JINST* **13** (2018), no. 05, P05011,
487 doi:10.1088/1748-0221/13/05/P05011, arXiv:1712.07158.
- 488 [79] **CMS** Collaboration, “Performance of missing energy reconstruction in 13 TeV pp
489 collision data using the CMS detector”, CMS Physics Analysis Summary
490 CMS-PAS-JME-16-004, CERN, 2016.
- 491 [80] **CMS** Collaboration, “Performance of missing transverse momentum in pp collisions at
492 $\sqrt{s} = 13$ TeV using the CMS detector”, CMS Physics Analysis Summary
493 CMS-PAS-JME-17-001, CERN, 2018.
- 494 [81] **SLAC** Collaboration, “Simulations”.
495 <https://theory.slac.stanford.edu/our-research/simulations>. (Retrieved Jul 25,
496 2017).
- 497 [82] **CMS** Collaboration, “Event generator tunes obtained from underlying event and
498 multiparton scattering measurements”, *Eur. Phys. J. C* **76** (2016) 155,
499 doi:10.1140/epjc/s10052-016-3988-x, arXiv:1512.00815.
- 500 [83] **CMS** Collaboration, “Extraction and validation of a new set of CMS PYTHIA8 tunes
501 from underlying-event measurements”, *Eur. Phys. J. C* **80** (2020) 4,
502 doi:10.1140/epjc/s10052-019-7499-4, arXiv:1903.12179.
- 503 [84] **CMS** Collaboration, “Investigations of the impact of the parton shower tuning in Pythia
504 8 in the modelling of $t\bar{t}$ at $\sqrt{s} = 8$ and 13 TeV”, CMS Physics Analysis Summary
505 CMS-PAS-TOP-16-021, CERN, 2016.
- 506 [85] **GEANT4** Collaboration, “GEANT4 — a simulation toolkit”, *Nucl. Instrum. Meth. A*
507 **506** (2003) 250, doi:10.1016/S0168-9002(03)01368-8.
- 508 [86] M. H. Seymour and M. Marx, “Monte Carlo Event Generators”, in *Proceedings, 69th*
509 *Scottish Universities Summer School in Physics: LHC Phenomenology (SUSSP69) 2012*,
510 p. 287. St.Andrews, Scotland, U.K., 2013. arXiv:1304.6677.
511 doi:10.1007/978-3-319-05362-2_8.
- 512 [87] T. Sjöstrand, S. Mrenna, and P. Z. Skands, “PYTHIA 6.4 Physics and Manual”, *JHEP*
513 **05** (2006) 026, doi:10.1088/1126-6708/2006/05/026, arXiv:hep-ph/0603175.
- 514 [88] F. Maltoni and T. Stelzer, “MadEvent: Automatic event generation with MadGraph”,
515 *JHEP* **02** (2003) 027, doi:10.1088/1126-6708/2003/02/027, arXiv:hep-ph/0208156.

- 516 [89] J. Alwall et al., “Comparative study of various algorithms for the merging of parton
517 showers and matrix elements in hadronic collisions”, *Eur. Phys. J. C* **53** (2008) 473,
518 doi:10.1140/epjc/s10052-007-0490-5, arXiv:0706.2569.
- 519 [90] J. Alwall et al., “The automated computation of tree-level and next-to-leading order
520 differential cross sections, and their matching to parton shower simulations”, *JHEP* **07**
521 (2014) 079, doi:10.1007/JHEP07(2014)079, arXiv:1405.0301.
- 522 [91] P. Nason, “A new method for combining NLO QCD with shower Monte Carlo
523 algorithms”, *JHEP* **11** (2004) 040, doi:10.1088/1126-6708/2004/11/040,
524 arXiv:hep-ph/0409146.
- 525 [92] S. Frixione, P. Nason, and C. Oleari, “Matching NLO QCD computations with parton
526 shower simulations: the POWHEG method”, *JHEP* **11** (2007) 070,
527 doi:10.1088/1126-6708/2007/11/070, arXiv:0709.2092.
- 528 [93] S. Alioli, P. Nason, C. Oleari, and E. Re, “A general framework for implementing NLO
529 calculations in shower Monte Carlo programs: the POWHEG BOX”, *JHEP* **06** (2010)
530 043, doi:10.1007/JHEP06(2010)043, arXiv:1002.2581.
- 531 [94] S. Frixione, P. Nason, and G. Ridolfi, “A positive-weight next-to-leading-order Monte
532 Carlo for heavy flavour hadroproduction”, *JHEP* **09** (2007) 126,
533 doi:10.1088/1126-6708/2007/09/126, arXiv:0707.3088.
- 534 [95] J. M. Campbell, R. K. Ellis, P. Nason, and E. Re, “Top-Pair Production and Decay at
535 NLO Matched with Parton Showers”, *JHEP* **04** (2015) 114,
536 doi:10.1007/JHEP04(2015)114, arXiv:1412.1828.
- 537 [96] S. Alioli, P. Nason, C. Oleari, and E. Re, “NLO single-top production matched with
538 shower in POWHEG: s - and t -channel contributions”, *JHEP* **09** (2009) 111,
539 doi:10.1088/1126-6708/2009/09/111, arXiv:0907.4076. [Erratum:
540 doi:10.1007/JHEP02(2010)011].
- 541 [97] E. Re, “Single-top Wt -channel production matched with parton showers using the
542 POWHEG method”, *Eur. Phys. J. C* **71** (2011) 1547,
543 doi:10.1140/epjc/s10052-011-1547-z, arXiv:1009.2450.
- 544 [98] T. Sjöstrand, S. Mrenna, and Z. S., Peter, “A Brief Introduction to PYTHIA 8.1”,
545 *Comput. Phys. Commun.* **178** (2008) 852, doi:10.1016/j.cpc.2008.01.036,
546 arXiv:0710.3820.
- 547 [99] T. Sjöstrand et al., “An introduction to PYTHIA 8.2”, *Comput. Phys. Commun.* **191**
548 (2015) 159, doi:10.1016/j.cpc.2015.01.024, arXiv:1410.3012.
- 549 [100] R. D. Ball et al., “Parton distributions for the LHC Run II”, *JHEP* **15** (2015) 40,
550 doi:10.1007/JHEP04(2015)040, arXiv:1410.8849.
- 551 [101] K. Melnikov and F. Petriello, “Electroweak gauge boson production at hadron colliders
552 through $O(\alpha_s^{**2})$ ”, *Phys. Rev. D* **74** (2006) 114017,
553 doi:10.1103/PhysRevD.74.114017, arXiv:hep-ph/0609070.
- 554 [102] M. Czakon and A. Mitov, “Top++: A Program for the Calculation of the Top-Pair
555 Cross-Section at Hadron Colliders”, *Comput. Phys. Commun.* **185** (2014) 2930,
556 doi:10.1016/j.cpc.2014.06.021, arXiv:1112.5675.

557 [103] “NNLO+NNLL top-quark-pair cross sections – ATLAS-CMS recommended predictions
558 for top-quark-pair cross sections using the Top++v2.0 program (M. Czakon, A. Mitov,
559 2013)”, <https://twiki.cern.ch/twiki/bin/view/LHCPhysics/TtbarNNLO>, 2022.
560 (Retrieved Dec 21, 2020).